

# VO<sub>2</sub> nanosheets: controlling the THz properties through strain engineering

Elsa Abreu<sup>§,1</sup> Mengkun Liu<sup>§,1</sup> Jiwei Lu<sup>§,2</sup> Kevin G. West,<sup>2</sup> Salinporn Kittiwatanakul,<sup>3</sup> Wenjing Yin,<sup>2</sup> Stuart A. Wolf,<sup>3,2</sup> and Richard D. Averitt<sup>1</sup>

<sup>1</sup>*Department of Physics, Boston University, Boston MA 02215, USA*

<sup>2</sup>*Department of Materials Science and Engineering,  
University of Virginia, Charlottesville VA 22904, USA*

<sup>3</sup>*Department of Physics, University of Virginia, Charlottesville VA 22904, USA*

We investigate far-infrared properties of strain engineered vanadium dioxide nanosheets through epitaxial growth on a (100)<sub>R</sub> TiO<sub>2</sub> substrate. The nanosheets exhibit large uniaxial strain leading to highly uniform and oriented cracks along the rutile c-axis. Dramatic anisotropy arises for both the metal-insulator transition temperature, which is different from the structural transition temperature along the c<sub>R</sub> axis, and the metallic state conductivity. Detailed analysis reveals a Mott-Hubbard like behavior along the rutile c<sub>R</sub> axis.

<sup>§</sup>contributed equally to this work

## I. INTRODUCTION

During the past five decades, vanadates have been intensely investigated from the point of view of clarifying the physics of metal-insulator transitions (MIT). Vanadium dioxide ( $\text{VO}_2$ ) is particularly intriguing, exhibiting a MIT with a conductivity decrease of over five orders of magnitude<sup>1</sup>. This is accompanied by a transition from a high temperature metallic rutile structure to an insulating monoclinic structure below the transition temperature. In bulk, the structural transition temperature,  $T_{St}^{bulk}$ , equals the metal-insulator transition temperature,  $T_{MI}^{bulk}$ , i.e.  $T_{St}^{bulk} \simeq T_{MI}^{bulk} \simeq 340\text{K}$ <sup>2</sup>. However,  $\text{VO}_2$  is not yet fully understood regarding the Mott-Hubbard or Peierls like nature of its MIT, though it is now generally accepted that a complete description requires explicit consideration of electron-electron correlations<sup>3,4</sup>. This is motivated in particular by the observed difference between the MIT and the structural transition temperatures, which provides significant evidence that the correlated conductivity behavior is independent of the structural phase<sup>5-7</sup>. Additionally, recent experimental studies highlight the multifunctional potential of  $\text{VO}_2$  including current or photoinduced phase changes (with the commensurate large tuning of the dielectric function) as well as integration with other technologies for applications including light detection and memory-based metamaterials<sup>8-10</sup>.

Strain engineering enables an additional degree of control of technologically relevant properties and provides a discriminatory capability towards obtaining fundamental insight into the microscopic origin of the macroscopic characteristics. Strain has been used to modify the MIT temperature in  $\text{VO}_2$  through direct application<sup>11</sup> or substrate-dependent application<sup>12,13</sup> of stress. For the present measurements, we utilize highly strained epitaxial  $(100)_R$   $\text{VO}_2$  thin films. The far-infrared conductivity is measured using non-contact polarization sensitive terahertz time-domain spectroscopy (THz-TDS) providing direct access to the coherent quasiparticle response along  $b_R$  or  $c_R$  by simply changing the sample orientation. Subsequent analysis indicates that the strain engineered tuning of vanadium  $a_{1g}$  and  $e_g^\pi$  orbitals controls the MIT transition temperature along  $c_R$ , which is different from the structural transition temperature. The origin of the observed conductivity anisotropy is also discussed, along with the potential for a technological application of strain engineered  $\text{VO}_2$  thin films as temperature switched far-infrared polarizers.

## II. EXPERIMENTS

The  $\sim 100\text{nm}$  and  $\sim 250\text{nm}$  thick  $\text{VO}_2$  films we investigated were deposited on rutile  $(100)_R$   $\text{TiO}_2$  substrates by temperature optimized sputtering from a vanadium target, using the reactive bias target ion beam deposition technique in an  $\text{Ar}+\text{O}_2$  gas mixture; details of the growth conditions can be found elsewhere<sup>14</sup>. The samples morphology was characterized by optical, atomic force (AFM) and scanning electron microscopies (SEM), and the film microstructure was analyzed by temperature dependent X-ray diffraction (XRD).

THz-TDS is a non-contact method to measure far-infrared conductivity. The conductivity anisotropy is easily determined from transmission of THz pulses for different sample orientations. In our case the output of a 1kHz 35fs Ti:Sapphire amplifier is used to generate nearly single-cycle THz pulses via optical rectification in a ZnTe crystal. We then employ a standard THz Time Domain Spectroscopy (THz TDS) setup to measure the transmission in the THz frequency range  $\sim 0.2 - 2.0\text{THz}$ <sup>15</sup>. By changing the sample orientation with respect to the THz pulse polarization we are able to monitor the transmission along different crystal axes.

$(100)_R$   $\text{TiO}_2$  has a large refractive index anisotropy in the THz range, partly caused by its characteristic rutile structure. Such an anisotropy in the  $(100)_R$   $\text{TiO}_2$  substrate makes it easy to distinguish transmitted THz signals with polarization parallel to  $c_R$  from THz signals with polarization perpendicular to  $b_R$  (Fig. 1(a)). Temperature dependent experimental characterization of the  $\text{TiO}_2$  substrate in the THz range, using our THz TDS setup, led to values of

$$\begin{aligned} n_e &\simeq 12.4 - 6 \times 10^{-4} \Delta T + 1.2i \\ n_o &\simeq 9.1 - 3 \times 10^{-4} \Delta T + 0.4i \end{aligned}$$

for the refractive index along  $c_R$  and  $b_R$ , respectively, in accordance with previous results<sup>16</sup>. Here,  $\Delta T$  stands for the temperature deviation with respect to room temperature. This approximation to the  $\text{TiO}_2$  complex refractive index holds between room temperature and 400K; it does not take into account the temperature dependence of the imaginary part, which is negligible for our purposes.

The conductivity of the  $\text{VO}_2$  film is extracted using the Fresnel equations, after experimental determination of the ratio of the THz transmission of the film to the THz transmission of a bare  $\text{TiO}_2$  substrate, used as a reference. THz TDS is thus a non-contact conductivity measurement, which allows one to quickly characterize the conductivity anisotropy in many samples with different thicknesses and substrates.

## III. RESULTS

### A. Characterization of the $\text{VO}_2$ nanosheets

Figure 2(a) is an AFM phase image of the 250nm film, showing periodic buckling and cracking of the film parallel to  $c_R$ , with inter-crack spacings on the order of  $1\mu m$ . The depth profile reveals nanosized ridges,  $\sim 15nm$  high, near the cracks. The SEM image in Fig. 2(b) confirms the  $\sim 250nm$  thickness of the film. It shows that the cracks' depth matches the film thickness and it gives an estimate of about  $30nm$  for their width. Such nanocracks were not detected by the AFM due to lack of tip sensitivity.

The optical images of the 100nm (Fig. 3(a)) and the 250nm (Fig. 3(b)) films confirm the  $\sim 1\mu m$  period spacing of the cracks along  $c_R$ . Also, the observed uniformity in the distribution of cracks is an indication that our films are strained in a highly homogeneous and oriented fashion. This crack distribution enables a comparison of our results with those of  $VO_2$  nanobeams, aligned along  $c_R$ <sup>13,17–20</sup>, although the dimensionality of our nanosheets gives access to the properties of strained  $VO_2$  along more than one axis. Such cracking uniformity was achieved by optimizing the growth conditions of the samples, in particular the growth temperature. In the case of our  $(100)_R$   $VO_2$  films the growth temperature was set to  $\sim 500^\circ C$ . Films grown at  $\sim 450^\circ C$  show cracking along different directions, which makes the characterization of the films along  $c_R$  less straightforward. All subsequent analysis is analogous for both the 100nm and the 250nm thick films. Unless otherwise specified the results will refer to the 100nm thick sample.

Detailed room temperature XRD of the  $VO_2$  film confirms the single crystal nature of the sample and yields the lattice parameters of the material (Fig. 4(a)). Comparing these values with those in the rutile phase of bulk  $VO_2$ <sup>21</sup> yields mismatches of  $-0.83\%$  along  $a_R$ ,  $-2.17\%$  along  $b_R$ , and  $1.41\%$  along  $c_R$ , indicative of a compressive strain along  $a_R$  and  $b_R$ , as opposed to a tensile strain along  $c_R$ . Such strain values along  $c_R$  are comparable to those achieved in one-dimensional  $VO_2$  nanobeams<sup>17</sup>. Bulk rutile  $TiO_2$  has larger lattice constants than bulk rutile  $VO_2$  along all directions so one would expect that both  $b_R$  and  $c_R$  would expand in  $(100)_R$   $VO_2$  films grown on a  $(100)_R$   $TiO_2$  substrate. However, our nanosheets show that the expansion along  $c_R$  surpasses the substrate clamping effect due to the  $b_R$ -axis, leading to a compressive strain in the  $ab_R$ -plane. This behavior is also observed in the 250nm thick film, with mismatches of  $-0.68\%$  along  $a_R^{250nm}$ ,  $-1.94\%$  along  $b_R^{250nm}$  and  $0.86\%$  along  $c_R^{250nm}$ .

Temperature dependent XRD results (Fig. 3(c)) show that a small  $a_R$ -axis expansion,  $\sim 0.1\%$ , occurs during the film's structural transition. This transition occurs at a temperature  $T_{St}^{film} \sim 340K \sim T_{St}^{bulk}$ , the same as in bulk, and shows the expected hysteric behavior. (From here on  $T_{St}$  will refer to both bulk and film structural transition temperatures.) The  $a_R$ -axis expansion in our strained sheet can be compared to that in bulk  $VO_2$ , estimated as  $\frac{a_R - b_M}{b_M} \simeq 0.6 - 0.8\%$ <sup>2,22</sup>, where  $b_M$  is the equivalent of  $a_R$  in the bulk monoclinic insulating structure. The order of magnitude difference between the lattice parameter variation in the film and that in bulk stems from the clamping effect of the rutile  $TiO_2$  substrate. This is consistent with the large strain observed in room temperature XRD, caused by the strong substrate clamping effect. The structural change exhibited at  $340K$  by our strained  $VO_2$  nanosheets is thus smaller than the change observed in bulk  $VO_2$ . Since  $VO_2$  shares the  $TiO_2$  rutile structure at high temperatures, the reduced structural change is expected to have an impact mainly on the low temperature  $VO_2$  film's structure. The temperature dependent  $(200)_R$   $2\theta$  plots from which the data in Fig. 3(c) were extracted are presented in Fig. 4(b). These raw data provide further support to our observation that the clamping effect due to the substrate is very strong, thereby preventing the development of significantly different structural phases in the strained  $VO_2$  film.

## B. THz Time Domain Spectroscopy

As shown in Fig. 1, upon increasing the temperature from the insulating to the metallic phase the THz peak transmission in the 100nm  $(100)_R$   $VO_2$  film drops by  $\sim 70\%$  along the  $c_R$ -axis and by  $\sim 15\%$  along the  $b_R$ -axis, and the THz peak transmission in the 250nm  $(100)_R$   $VO_2$  film drops by  $\sim 85\%$  along the  $c_R$ -axis and by  $\sim 15\%$  along the  $b_R$ -axis. Figure 1(b) shows the transmission anisotropy in our 250nm  $VO_2$  sample, normalized to its low temperature value along each axis ( $b_R$  and  $c_R$ ). This representation highlights the dramatic difference between the low temperature transmission along  $b_R$  and that along  $c_R$ , thereby illustrating the potential of strained  $VO_2$  films as temperature tunable THz polarizing beamsplitters.

Figure 5(a) shows the temperature dependent far infrared conductivity, obtained from the transmission data, for the 100nm  $(100)_R$   $VO_2$  nanosheet. The conductivity along  $c_R$  shows a clear transition from the insulating to the metallic state with a narrow hysteresis, which is indicative of the high quality of the film. In the metallic state the conductivity is  $\sigma_{c_R} \sim 5650(\Omega cm)^{-1}$ , comparable to bulk single crystal values<sup>1</sup>. The MIT along  $c_R$  occurs at a temperature  $T_{MI}^{c_R} \simeq 365^\circ K$ .  $T_{MI}^{c_R}$  is significantly larger than both the structural transition temperature and the bulk MIT temperature,  $T_{St} \sim T_{MI}^{bulk} \sim 340K$ . Our  $VO_2$  films therefore exhibit, along  $c_R$ , a  $\sim 25K$  temperature difference between the structural and the metal-insulator transition temperatures. The combination of the quasi three dimensionality of our nanosheets, which enables a direct measurement of the strain along the three crystal axes through XRD analysis, with the polarization sensitivity of THz spectroscopy is the key to identifying this distinction between the two transition temperatures.

The conductivity along  $b_R$  also exhibits a transition (see inset of Fig. 5(a)), which occurs at  $T_{MI}^{b_R} \simeq 340^\circ K$ . Along this direction we therefore observe that the structural and metal-insulator transition temperatures are the same,  $T_{MI}^{b_R} \sim T_{St} \sim T_{MI}^{bulk}$ . However, the conductivity along  $b_R$  reaches a high temperature value about 30 times smaller

than the high temperature conductivity along  $c_R$ . This strong conductivity anisotropy will be addressed later in the text.

THz TDS results for the 250nm thick sample (Fig. 6) indicate that its transport properties are similar to that of the 100nm sample. In particular, the high temperature conductivity along  $c_R$  remains as good as in bulk  $\text{VO}_2$  single crystals<sup>1</sup> while  $T_{MI}^{c_R} \simeq 365\text{K} > T_{MI}^{bulk}$ . The high temperature conductivity along  $b_R$  is very low,  $< 100(\Omega\text{cm})^{-1}$ , and the transition temperature can only be estimated at  $T_{MI}^{b_R} \simeq 340\text{K}$ , consistent with  $T_{MI}^{bulk}$  and  $T_{St}$  and in line with what is observed in the 100nm sample (Fig. 5(a)).

#### IV. DISCUSSION

Understanding the contribution of the V3d orbitals to the electronic properties is crucial in order to explain the large material anisotropy in  $T_{MI}$ <sup>23</sup>. A splitting of the 5-fold degenerate 3d states occurs due to the octahedral coordination of the V atoms, resulting in a higher energy doubly degenerate  $e_g$  level and a lower energy triply degenerate  $t_{2g}$  level. Trigonal distortion further splits the  $t_{2g}$  levels leading to an upshifted doubly degenerate  $e_g^\pi$  state, responsible for conduction in the  $ab_R$ -plane, while downshifting a non-degenerate  $c_R$ -oriented  $a_{1g}$  state (Fig. 5(b)). Recent cluster Dynamical Mean Field Theory (cDMFT) calculations<sup>4</sup>, which include the effect of a  $\pm 2\%$  strain along  $c_R$ , have demonstrated that a tensile strain along  $c_R$  narrows the  $a_{1g}$  derived band and leads to a compressive strain in the  $ab_R$ -plane, which uplifts the  $e_g^\pi$  band (Fig. 5(c)). In the Mott picture the energy increase of  $e_g^\pi$  electrons reduces the screening of electrons residing in the  $a_{1g}$  band, thereby enhancing the effect of correlations (i.e. increasing the screened Hubbard U). This results in an increase of the insulating band gap which opens, below  $T_{MI}$ , between the bonding  $a_{1g}$  and the anti-bonding  $e_g^\pi$  levels, therefore leading to an increased  $T_{MI}$  along  $c_R$ <sup>24,25</sup>.

The epitaxial strain in our film can be decomposed into a uniaxial tensile strain along  $c_R$  and a uniaxial compressive strain along  $b_R$ . Along  $c_R$ ,  $T_{MI}^{c_R} \sim 365\text{K} > T_{MI}^{bulk}$ , in line with previous experimental results<sup>11</sup>, while  $\sigma_{c_R}$  remains comparable to the best single crystal values<sup>1</sup>. These results agree with the Mott picture above, where the increased lattice spacing along  $c_R$  further increases the ratio of Coulomb repulsion to the inter-atomic hopping integral, thereby destabilizing the metallic phase and increasing  $T_{MI}$ . The Peierls picture predicts a decrease in  $T_{MI}^{c_R}$  with tensile strain along  $c_R$ , thus failing to describe our results along that axis<sup>4</sup>. Also contrary to the Peierls-driven MIT scenario along  $c_R$  is the fact that the structural transition occurs at a temperature  $T_{St} \sim 340\text{K}$ , 25K lower than  $T_{MI}^{c_R}$ : in a Peierls picture both transitions would be expected to occur at the same temperature. In contrast to what happens along  $c_R$ , the results along  $b_R$ , where  $T_{MI}^{b_R} = T_{St}$ , are compatible with a Peierls-driven MIT scenario.

As mentioned above, our samples are cracked along  $c_R$ . The occurrence of such cracks is common in  $\text{VO}_2$ , in both bulk and strained samples<sup>26,27</sup>, and this has prevented accurate measurements of the DC conductivity in this material in the direction perpendicular to  $c_R$ . Hindered quasiparticle motion along  $b_R$  due to the presence of  $c_R$  oriented cracks is the most likely explanation for the reduced value of  $\sigma_{b_R}$  in our films. However, a different scenario could arise in the THz range. Due to the small value of the far-infrared carrier mean free path ( $\sim \text{\AA}^{28}$ ) compared to DC, the  $\sim 1\text{ps}$  long THz field should be able to couple to the material along  $b_R$  despite the cracks along  $c_R$ . According to this picture, the uniaxial compressive strain along  $b_R$  would play a significant role in reducing  $\sigma_{b_R}$ , compared to  $\sigma_{c_R}$ , while keeping  $T_{MI}^{b_R} = T_{MI}^{bulk} = T_{St}$ . Given the orbitals orientation, conductivity in the  $ab_R$ -plane is mediated by the  $e_g^\pi$  orbitals whose energy is controlled by the overlap between O2p and V3d orbitals<sup>24</sup>. Low conductivity behavior in the compressed  $ab_R$ -plane for  $T > T_{MI}$  would then arise from the  $e_g^\pi$  states being higher in energy than in the unstrained case, which reduces their overlap with the Fermi level (Fig. 5C).  $\text{VO}_2$  nanosheets that remain uncracked while maintaining a high level of strain along  $b_R$  must be investigated in order to clarify the role of the  $e_g^\pi$  orbitals on the high temperature value of  $\sigma_{b_R}$ , thereby also clarifying the nature of the MIT along that axis.

Our strained  $\text{VO}_2$  films on a  $\text{TiO}_2$  substrate have been shown to enable the separation of the far-infrared signal's polarization components both in time and intensity. The temperature dependent THz conductivity of strained  $\text{VO}_2$  nanosheets (Figs. 5(a) and 6) shows that incident light polarized parallel to  $b_R$  is transmitted through  $\text{VO}_2$  at both low and high temperatures, whereas incident light polarized parallel to  $c_R$  is transmitted through  $\text{VO}_2$  at low temperatures but reflected at high temperatures. Our strained  $\text{VO}_2$  single crystal nanosheets can thus be thought of as temperature switchable far-infrared polarizing beamsplitters.

#### V. PHASE DIAGRAM

Finally, it is interesting to map the strain of our film onto the  $\text{VO}_2$  phase diagram in Fig. 7, constructed based on past studies of  $\text{VO}_2$  as a function of temperature, pressure<sup>17,29</sup> and doping<sup>30-33</sup>. In general, it is not trivial to map the effect of doping onto that of pressure. This was initiated by Pouget *et al.*, who found a one-to-one correspondence between Cr-doping and the application of uniaxial stress along  $[110]_R$ <sup>29,32</sup>. Other doping experiments tend to indicate that doping ions with radii smaller than  $\text{V}^{4+}$  lead to an increase in  $T_{MI}$  whereas those with larger radii have the opposite effect<sup>34</sup>. This is similar to what happens in  $\text{V}_2\text{O}_3$ , a canonical Mott insulator<sup>35</sup>.



Figure 7 compiles previous experimental results obtained on  $\text{VO}_2$  under different pressure<sup>17,29</sup> and doping<sup>30–33</sup> conditions.  $P = 0$  corresponds to atmospheric pressure. The application of hydrostatic pressure<sup>1,40,41</sup> cannot be easily interpreted in terms of its influence on the conductivity nor on  $T_{MI}$  along individual axes of the crystalline structure, which corresponds to the main focus of our study. We therefore do not include hydrostatic pressure data in the phase diagram of Fig. 7. The dashed white lines delimit the region of the phase diagram where uniaxial pressure was applied along  $[001]_R$  (up to  $12\text{kbar}$ ), both for compression ( $P < 0$ ) and tension ( $P > 0$ ), and along  $[110]_R$  (up to  $\sim 1.2\text{kbar}$ ), only for compression ( $P > 0$ ). Within the rectangle, the dashed red line represents  $T_{MI}^{c_R}$  versus stress along  $c_R$ ,  $[001]_R$ , while the solid red line represents  $T_{MI}^{c_R}$  versus stress in the  $ab_R$ -plane,  $[110]_R$ . The dashed black lines separate different insulating phases within the low temperature monoclinic phase. The dash-dotted line between phases  $M_2$  and  $M_4$  is a conjecture<sup>30,33</sup>. Note that apart from the dashed red line, relative to stress along  $[001]_R$ , all the information in the diagram refers to stress along  $[110]_R$ . The white oval indicates the phase space characteristic of our  $(100)_R$   $\text{VO}_2$  samples. The uniaxial stress on our films along  $[110]_R$  has been estimated, respectively for the  $100\text{nm}$  and the  $250\text{nm}$  samples, to  $\sim 20.9\text{kbar}$  and  $\sim 18.5\text{kbar}$ , based on the measured  $-2.32\%$  and  $-2.06\%$  mismatch along  $(110)_R$ , and on a Young modulus of  $\sim 900\text{kbar}$ <sup>42</sup>. These uniaxial stress values are higher than ever reported, to our knowledge, for uniaxial stress on  $\text{VO}_2$ .

The dependence of  $T_{MI}$  on doping, studied in  $\text{V}_{1-x}\text{M}_x\text{O}_2$  compounds, can be approximately mapped onto its dependence on applied pressure. Reduction of  $\text{V}^{4+}$  is achieved using  $\text{M} = \text{Nb, Mo, W, Ta, Re, Ir, F, Ti, Os, Ru, Tc}$ , etc., with formal charges of  $+4$ ,  $+5$  or  $+6$ <sup>23,32,34,43–54</sup>. The effect on  $T_{MI}$  is similar to that of negative (compressive) stress along  $[001]_R$ , yielding  $dT_{MI}/dx = -0.3 \sim -28\text{K/at.}\%M$ . Oxidation of  $\text{V}^{4+}$  is achieved using  $\text{M} = \text{Cr, Al, Fe, Ga, Ge, Sn, Mn, Co}$ , etc., with formal charges of  $+3$  or  $+4$ <sup>23,31–34,39,43,55–59</sup>. The effect on  $T_{MI}$  is similar to that of positive (tensile) stress along  $[001]_R$ , yielding  $dT_{MI}/dx = 0 \sim 13\text{K/at.}\%M$ .

Our results, indicated by the white oval in the phase diagram of Fig. 7, are comparable to those of Everhart *et al.*, where an anisotropy of about two orders of magnitude is observed in the metallic phase of bulk  $\text{VO}_2$  single crystals doped with iron at  $0.076\%$ <sup>37</sup>. Our estimate of the stress puts our samples in a region of the phase diagram where  $T_{MI}$  increases with stress, and where a two phase behavior is expected above  $T_{MI}$ . This is consistent with our observation of both insulating ( $T < T_{MI}^{c_R}$ ) and metallic ( $T > T_{MI}^{c_R}$ ) values of  $\sigma_{c_R}$  in the same rutile structure, above  $T_{St}$ . The independence of the conductivity behavior from the structural phase has been reported before<sup>5–7</sup>, though relative to monoclinic structures. As for the low temperature structure,  $M_4$  or rutile seem to be the most likely candidates, although we cannot distinguish between the two.  $M_1$ ,  $M_2$  and  $M_3/T$  are all structurally too far from rutile<sup>20,30,31</sup> to lead to the results shown in Fig. 3C, and they are located in different regions of the phase diagram, as seen in Fig. 7. These observations, along with the strong conductivity anisotropy exhibited by our strained nanosheets, are indicative of a more complex behavior of  $\text{VO}_2$ , beyond the currently accepted doping and strain dependence of its structural and transport properties (Fig. 7).

Coming back to the conductivity measured in our strained nanosheets, it is important to point out that its anisotropy is unexpectedly large compared to previous experimental observations and theoretical calculations on  $\text{VO}_2$  samples<sup>12,36–39</sup>. The anisotropy in the DC conductivity,  $\frac{\sigma_{c_R}}{\sigma_{b_R}}$  or  $\frac{\sigma_{c_R}}{\sigma_{a_R}}$ , in undoped  $\text{VO}_2$  samples is generally  $>1$  for  $T < T_{MI}$  but can take many different values for  $T > T_{MI}$  (Table I). Differences in sample quality and stoichiometry as well as in conductivity measurement techniques surely affect the results, but variations in geometry and internal strain / cracking are likely to also have an effect on the anisotropy of metallic  $\text{VO}_2$ .

Tables I and II present a complete and up to date review, to our knowledge, of the experimental and theoretical data on conductivity anisotropy in  $\text{VO}_2$ , including the effect of externally applied stress. Table I includes the results for the conductivity anisotropy, above and below  $T_{MI}$ , when no external stress is applied<sup>12,36–39,60–64</sup>. Table II presents several results for the strain induced variation of  $T_{MI}$  and of the conductivity in  $\text{VO}_2$ , for situations where hydrostatic or uniaxial pressure is applied to the samples<sup>1,7,11,12,17,29,40,41,65–67</sup>.

As seen in tables I and II, in most situations where uniaxial pressure is applied the conductivity is measured along  $c_R$ , the only axis along which it is well defined due to geometry constraints of the samples or to cracking. Few studies determine the conductivity along  $a_R$  or  $b_R$  as a function of applied pressure. In general, it is agreed that (i) an applied uniaxial compressive (tensile) stress along the  $c_R$ -axis leads to an increased (decreased) conductivity at  $T > T_{MI}$ ; (ii) an applied uniaxial compressive (tensile) stress along the  $c_R$ -axis leads to a decreased (increased)  $T_{MI}$  (the axis along which  $T_{MI}$  is measured is not always specified); (iii) a small uniaxial stress applied along the  $[110]_R$  direction has no significant effect on the conductivity nor  $T_{MI}$  along  $c_R$  but it promotes a phase transition between different monoclinic structures ( $M_1$ ,  $M_2$ ,  $T/M_3$ ,  $M_4$ ), in the insulating phase<sup>29–31</sup>. Further experiments are needed in order to systematically measure the conductivity along  $a_R$  or  $b_R$  under (i) an applied uniaxial stress along  $a_R$  or  $b_R$ ; (ii) an applied uniaxial stress along  $c_R$ ; (iii) hydrostatic pressure. Also, clear criteria for distinguishing  $T_{MI}$  from  $T_{St}$  would be extremely valuable to help draw a more accurate and complete phase diagram, in line with what has been attempted in previous studies<sup>5–7</sup>. The highly oriented strain across a quasi three dimensional structure, achieved in epitaxially grown  $\text{VO}_2$  nanosheets, offers an extraordinary versatility and potential for investigation of these issues.

Theoretically, several pictures have been suggested to explain the anisotropy in (unstrained)  $\text{VO}_2$ : (1) a two band

model description of 3d electrons, within the framework of the Goodenough model, predicts a non conducting  $ab_R$ -plane for  $T > T_{MI}$ , any residual conductivity in that plane being due to the overlap of O2p and V3d orbitals<sup>23,24</sup>; (2) LDA calculations by Allen's group predict the structural distortion to be the main force driving the MIT in VO<sub>2</sub>, following a simple Peierls picture<sup>68</sup>; (3) a three-band Hubbard model, suggested by Tanaka *et al.*, predicts a one dimensional conducting phase along  $c_R$  for  $T < T_{MI}$  and an isotropically conducting phase for  $T > T_{MI}$ <sup>69</sup>; (4) LDA+cDMFT calculations by Biermann *et al.* suggest that electron correlations within the  $e_g^\pi$  levels are weaker than those along the  $a_{1g}$  ones<sup>3</sup>; (5) subsequent LDA+cDMFT calculations by Kotliar's group, which include a moderate degree of uniaxial strain, suggest that electronic correlations are the main driving force in the MIT, and that the rutile phase itself should be able to support both metallic and insulating electronic behavior<sup>4</sup>; (6) Liebsch *et al.* compared the LDA+U, DMFT and GW methods and found that none of them provides a full description of VO<sub>2</sub>, namely of the development of the insulating gap below  $T_{MI}$ <sup>70</sup>. Nonetheless, most of the calculations based on unstrained VO<sub>2</sub> samples agree that (i)  $a_{1g}$  and  $e_g^\pi$  states can be regarded as nearly independent; (ii) the conductivity is expected to be of predominantly  $a_{1g}$  behavior for  $T < T_{MI}$  and nearly isotropic for  $T > T_{MI}$ ; (iii) electron correlations should be included in the model, mainly in the  $c_R$  oriented  $a_{1g}$  levels. Our results agree with (i) and (iii), while strain induced cracking prevents the accurate description of the effect mentioned in (ii). Further theoretical investigations should take into account not only strain<sup>4</sup> but also the oxygen degrees of freedom, in order to provide a more accurate description of the O2p and V3d orbitals overlap, most relevant for describing the conductivity in the  $ab_R$ -plane, and of the subsequent cracking along  $c_R$ . Such estimates would be adequate for a quantitative, rather than merely qualitative, comparison with our experimental data.

## VI. CONCLUSION

In summary, we have observed a large anisotropy of the properties of strained 100nm and 250nm thick VO<sub>2</sub> nanosheets. The increased value of  $T_{MI}^{c_R}$  compared to  $T_{St}$  is a clear signature of a Mott- rather than Peierls-driven MIT along  $c_R$ . An  $e_g^\pi$  orbital tuning picture is proposed to explain the reduced value of the high temperature  $\sigma_{b_R}$ , although a crack induced conductivity decrease cannot be conclusively ruled out. Additional experiments are needed in order to clarify the mechanism of the phase transition in strained VO<sub>2</sub>, mainly in the direction perpendicular to  $c_R$ . This would allow the development of a more comprehensive phase diagram for this material. In general, epitaxial strain engineering is a powerful tool which has the potential to enable careful tuning of the metal-insulator transition in numerous other correlated electron materials, thereby providing a viable route towards technologically relevant multifunctionality and increased understanding of the microscopic origin of the MIT.

## ACKNOWLEDGMENTS

We thank Kebin Fan and Wei Zhang for SEM sample characterization. We acknowledge support from DOE - Basic Energy Sciences under Grant No. DE-FG02-09ER46643 (E.A., M.L., R.D.A.). E. Abreu acknowledges support from Fundação para a Ciência e a Tecnologia, Portugal, through a doctoral degree fellowship (SFRH/ BD/ 47847/ 2008).

- 
- <sup>1</sup> L. A. Ladd and W. Paul, Solid State Communications **7**, 425 (1969)
  - <sup>2</sup> G. Andersson, Acta Chemica Scandinavica **10**, 623 (1956)
  - <sup>3</sup> S. Biermann, A. Poteryaev, A. Lichtenstein, and A. Georges, Physical Review Letters **94**, 026404 (Jan. 2005), ISSN 0031-9007, <http://link.aps.org/doi/10.1103/PhysRevLett.94.026404>
  - <sup>4</sup> B. Lazarovits, K. Kim, K. Haule, and G. Kotliar, Physical Review B **81**, 115117 (Mar. 2010), ISSN 1098-0121, <http://link.aps.org/doi/10.1103/PhysRevB.81.115117>
  - <sup>5</sup> H.-T. Kim, Y. W. Lee, B.-J. Kim, B.-G. Chae, S. J. Yun, K.-Y. Kang, K.-J. Han, K.-J. Yee, and Y.-S. Lim, Physical Review Letters **97**, 266401 (Dec. 2006), ISSN 0031-9007, <http://link.aps.org/doi/10.1103/PhysRevLett.97.266401>
  - <sup>6</sup> M. Qazilbash, A. Tripathi, A. Schafgans, B.-J. Kim, H.-T. Kim, Z. Cai, M. Holt, J. Maser, F. Keilmann, O. Shpyrko, and D. Basov, Physical Review B **83**, 165108 (Apr. 2011), ISSN 1098-0121, <http://link.aps.org/doi/10.1103/PhysRevB.83.165108>
  - <sup>7</sup> E. Arcangeletti, L. Baldassarre, D. Di Castro, S. Lupi, L. Malavasi, C. Marini, A. Perucchi, and P. Postorino, Physical Review Letters **98**, 196406 (May 2007), ISSN 0031-9007, <http://link.aps.org/doi/10.1103/PhysRevLett.98.196406>
  - <sup>8</sup> H.-T. Kim, B.-G. Chae, D.-H. Youn, G. Kim, K.-Y. Kang, S.-J. Lee, K. Kim, and Y.-S. Lim, Applied Physics Letters **86**, 242101 (2005), ISSN 00036951, <http://link.aip.org/link/APPLAB/v86/i24/p242101/s1&Agg=doi>
  - <sup>9</sup> T. Driscoll, H.-T. Kim, B.-G. Chae, B.-J. Kim, Y.-W. Lee, N. M. Jokerst, S. Palit, D. R. Smith, M. Di Ventura, and D. N. Basov, Science **325**, 1518 (Sep. 2009), ISSN 1095-9203, <http://www.ncbi.nlm.nih.gov/pubmed/19696311>
  - <sup>10</sup> D. Hilton, R. Prasankumar, S. Fourmaux, A. Cavalleri, D. Brassard, M. El Khakani, J. Kieffer, A. Taylor, and R. Averitt, Physical Review Letters **99**, 226401 (Nov. 2007), ISSN 0031-9007, <http://link.aps.org/doi/10.1103/PhysRevLett.99.226401>

- <sup>11</sup> Y. Muraoka, Y. Ueda, and Z. Hiroi, *Journal of Physics and Chemistry of Solids* **63**, 965 (Aug. 2002), ISSN 00223697, <http://linkinghub.elsevier.com/retrieve/pii/S0022369702000987>
- <sup>12</sup> J. Lu, K. G. West, and S. a. Wolf, *Applied Physics Letters* **93**, 262107 (2008), ISSN 00036951, <http://link.aip.org/link/APPLAB/v93/i26/p262107/s1&Agg=doi>
- <sup>13</sup> S. Zhang, J. Y. Chou, and L. J. Lauhon, *Nano Letters* **9**, 4527 (Dec. 2009), ISSN 1530-6992, <http://www.ncbi.nlm.nih.gov/pubmed/19902918>
- <sup>14</sup> K. G. West, J. Lu, J. Yu, D. Kirkwood, W. Chen, Y. Pei, J. Claassen, and S. a. Wolf, *Journal of Vacuum Science & Technology A* **26**, 133 (2008), ISSN 07342101, <http://link.aip.org/link/JVTAD6/v26/i1/p133/s1&Agg=doi>
- <sup>15</sup> P. Jepsen, D. Cooke, and M. Koch, *Laser & Photonics Reviews* **5**, 124 (Jan. 2011), ISSN 18638880, <http://doi.wiley.com/10.1002/lpor.201000011>
- <sup>16</sup> C. Jördens, M. Scheller, M. Wichmann, M. Mikulics, K. Wiesauer, and M. Koch, *Applied optics* **48**, 2037 (Apr. 2009), ISSN 1539-4522, <http://www.ncbi.nlm.nih.gov/pubmed/19363540>
- <sup>17</sup> J. Cao, E. Ertekin, V. Srinivasan, W. Fan, S. Huang, H. Zheng, J. W. L. Yim, D. R. Khanal, D. F. Ogletree, J. C. Grossman, and J. Wu, *Nature Nanotechnology* **4**, 732 (Sep. 2009), ISSN 1748-3387, <http://www.nature.com/doi/10.1038/nnano.2009.266>
- <sup>18</sup> J. Wu, Q. Gu, B. S. Guiton, N. P. de Leon, L. Ouyang, and H. Park, *Nano Letters* **6**, 2313 (Oct. 2006), ISSN 1530-6984, <http://www.ncbi.nlm.nih.gov/pubmed/17034103>
- <sup>19</sup> J. I. Sohn, H. J. Joo, D. Ahn, H. H. Lee, A. E. Porter, K. Kim, D. J. Kang, and M. E. Welland, *Nano Letters* **9**, 3392 (Oct. 2009), ISSN 1530-6992, <http://www.ncbi.nlm.nih.gov/pubmed/19785429>
- <sup>20</sup> A. C. Jones, S. Berweger, J. Wei, D. Cobden, and M. B. Raschke, *Nano Letters* **10**, 1574 (May 2010), ISSN 1530-6992, <http://www.ncbi.nlm.nih.gov/pubmed/20377237>
- <sup>21</sup> D. B. McWhan, M. Marezio, J. P. Remeika, and P. D. Dernier, *Physical Review B* **10**, 490 (1974)
- <sup>22</sup> D. Kucharczyk and T. Niklewski, *Journal of Applied Crystallography* **12**, 370 (1979)
- <sup>23</sup> J. Goodenough, *Journal of Solid State Chemistry* **3**, 490 (Nov. 1971), ISSN 00224596, <http://linkinghub.elsevier.com/retrieve/pii/0022459671900910>
- <sup>24</sup> V. Eyert, *Annalen der Physik (Leipzig)* **11**, 650 (Oct. 2002), ISSN 00033804, [http://doi.wiley.com/10.1002/1521-3889\(200210\)11:9<650::AID-ANDP650>3.0.CO;2-K](http://doi.wiley.com/10.1002/1521-3889(200210)11:9<650::AID-ANDP650>3.0.CO;2-K)
- <sup>25</sup> A. Zylbersztejn and M. N. F., *Physical Review B* **11**, 4383 (1975)
- <sup>26</sup> C. N. Berglund and H. J. Guggenheim, *Physical Review* **185**, 1022 (1969)
- <sup>27</sup> K. Nagashima, T. Yanagida, H. Tanaka, and T. Kawai, *Physical Review B* **74**, 172106 (Nov. 2006), ISSN 1098-0121, <http://link.aps.org/doi/10.1103/PhysRevB.74.172106>
- <sup>28</sup> M. Qazilbash, K. Burch, D. Whisler, D. Shrekenhamer, B. Chae, H. Kim, and D. Basov, *Physical Review B* **74**, 205118 (Nov. 2006), ISSN 1098-0121, <http://link.aps.org/doi/10.1103/PhysRevB.74.205118>
- <sup>29</sup> J. P. Pouget, H. Launois, J. P. D'Haenens, P. Merenda, and T. M. Rice, *Physical Review Letters* **35**, 873 (1975)
- <sup>30</sup> J. B. Goodenough and H. Y.-P. Hong, *Physical Review B* **8**, 1323 (1973)
- <sup>31</sup> M. Marezio, D. B. McWhan, J. P. Remeika, and P. D. Dernier, *Physical Review B* **5**, 2541 (1972)
- <sup>32</sup> J. P. Pouget and H. Launois, *Journal de Physique Colloques* **37**, C4 (1976)
- <sup>33</sup> P. Villeneuve, G., Drillon, M., Hagenmuller, *Materials Research Bulletin* **8**, 1111 (1973)
- <sup>34</sup> J. Macchesney and H. Guggenheim, *Journal of Physics and Chemistry of Solids* **30**, 225 (Feb. 1969), ISSN 00223697, <http://linkinghub.elsevier.com/retrieve/pii/0022369769903035>
- <sup>35</sup> D. B. McWhan, T. M. Rice, and J. P. Remeika, *Physical Review Letters* **23**, 1384 (1969)
- <sup>36</sup> H. J. Barker, A. S., Verleur, H. W., Guggenheim, *Physical Review Letters* **17**, 1286 (1966)
- <sup>37</sup> J. B. Everhart, C. R., MacChesney, *Journal of Applied Physics* **39**, 2872 (1968)
- <sup>38</sup> P. F. Bongers, *Solid State Communications* **3**, 275 (1965)
- <sup>39</sup> K. Kosuge, *Journal of the Physical Society of Japan* **22**, 551 (1967)
- <sup>40</sup> C. H. Neuman, A. W. Lawson, and R. F. Brown, *The Journal of Chemical Physics* **41**, 1591 (1964)
- <sup>41</sup> C. N. Berglund and A. Jayaraman, *Physical Review* **185**, 1034 (1969)
- <sup>42</sup> N. Sepulveda, A. Rua, R. Cabrera, and F. Fernandez, *Applied Physics Letters* **92**, 191913 (2008), ISSN 00036951, <http://link.aip.org/link/APPLAB/v92/i19/p191913/s1&Agg=doi>
- <sup>43</sup> F. Bêteille and J. Livage, *Journal of Sol-Gel Science and Technology* **13**, 915 (1998)
- <sup>44</sup> G. Villeneuve, A. Bordet, A. Casalot, J. Pouget, H. Launois, and P. Lederer, *Journal of Physics and Chemistry of Solids* **33**, 1953 (Jul. 1972), ISSN 00381098, <http://linkinghub.elsevier.com/retrieve/pii/003810987291191X>
- <sup>45</sup> C. Piccirillo, R. Binions, and I. P. Parkin, *European Journal of Inorganic Chemistry* **2007**, 4050 (Sep. 2007), ISSN 14341948, <http://doi.wiley.com/10.1002/ejic.200700284>
- <sup>46</sup> M. Hörlin, T., Niklewski, T., Nygren, *Materials Research Bulletin* **8**, 179 (1973)
- <sup>47</sup> K. Holman, T. McQueen, A. Williams, T. Klimczuk, P. Stephens, H. Zandbergen, Q. Xu, F. Ronning, and R. Cava, *Physical Review B* **79**, 245114 (Jun. 2009), ISSN 1098-0121, <http://link.aps.org/doi/10.1103/PhysRevB.79.245114>
- <sup>48</sup> M. Nygren, M., Israelsson, *Materials Research Bulletin* **4**, 881 (1969)
- <sup>49</sup> B. G. Chae, H. T. Kim, and S. J. Yun, *Electrochemical and Solid-State Letters* **11**, D53 (2008), ISSN 10990062, <http://link.aip.org/link/ESLEF6/v11/i6/pD53/s1&Agg=doi>
- <sup>50</sup> O. Sävborg and M. Nygren, *Physica Status Solidi (a)* **43**, 645 (Oct. 1977), ISSN 00318965, <http://doi.wiley.com/10.1002/pssa.2210430236>
- <sup>51</sup> M. Bayard, *Journal of Solid State Chemistry* **12**, 41 (Jan. 1975), ISSN 00224596, <http://linkinghub.elsevier.com/retrieve/pii/0022459675901760>

- <sup>52</sup> I. K. Kristensen, *Journal of Applied Physics* **39**, 5341 (1968)
- <sup>53</sup> B.-O. Marinder and A. Magnéli, *Acta Chemica Scandinavica* **11**, 1635 (1957)
- <sup>54</sup> Q. Gu, A. Falk, J. Wu, L. Ouyang, and H. Park, *Nano Letters* **7**, 363 (Mar. 2007), ISSN 1530-6984, <http://www.ncbi.nlm.nih.gov/pubmed/17256915>
- <sup>55</sup> M. Drillon and G. Villeneuve, *Materials Research Bulletin* **9**, 1199 (1974)
- <sup>56</sup> E. Pollert, G. Villeneuve, F. Ménil, and P. Hagenmuller, *Materials Research Bulletin* **11**, 159 (1976)
- <sup>57</sup> F. Pintchovski, W. S. Glaunsinger, and A. Navrotsky, *Journal of the Physics and Chemistry of Solids* **39**, 941 (1978)
- <sup>58</sup> I. Kitahiro and A. Watanabe, *Japanese Journal of Applied Physics* **6**, 1023 (1967)
- <sup>59</sup> M.-H. Lee, M.-G. Kim, and H.-K. Song, *Thin Solid Films* **290-291**, 30 (1996)
- <sup>60</sup> H. W. Verleur, A. S. Barker, and C. N. Berglund, *Physical Review* **172**, 788 (1968)
- <sup>61</sup> a. Continenza, S. Massidda, and M. Posternak, *Physical Review B* **60**, 15699 (Dec. 1999), ISSN 0163-1829, <http://link.aps.org/doi/10.1103/PhysRevB.60.15699>
- <sup>62</sup> R. J. O. Mossaneck and M. Abbate, *Journal of Physics: Condensed Matter* **19**, 346225 (Aug. 2007), ISSN 0953-8984, <http://stacks.iop.org/0953-8984/19/i=34/a=346225?key=crossref.097329a8505cf348ca29f0117d3a15db>
- <sup>63</sup> S. Lysenko, V. Vikhnin, F. Fernandez, A. Rua, and H. Liu, *Physical Review B* **75**, 075109 (Feb. 2007), ISSN 1098-0121, <http://link.aps.org/doi/10.1103/PhysRevB.75.075109>
- <sup>64</sup> J. Tomczak and S. Biermann, *Physical Review B* **80**, 1 (Aug. 2009), ISSN 1098-0121, <http://link.aps.org/doi/10.1103/PhysRevB.80.085117>
- <sup>65</sup> S. Minomura and H. Hagasaki, *Journal of the Physical Society of Japan* **19**, 131 (1964)
- <sup>66</sup> J. M. Gregg and R. M. Bowman, *Applied Physics Letters* **71**, 3649 (1997), ISSN 00036951, <http://link.aip.org/link/APPLAB/v71/i25/p3649/s1&Agg=doi>
- <sup>67</sup> J. Sakai, *Journal of Applied Physics* **104**, 073703 (2008), ISSN 00218979, <http://link.aip.org/link/JAPIAU/v104/i7/p073703/s1&Agg=doi>
- <sup>68</sup> R. M. Wentzcovitch, W. W. Schulz, and P. B. Allen, *Physical Review Letters* **72**, 3389 (1994)
- <sup>69</sup> A. Tanaka, *Journal of the Physics Society Japan* **72**, 2433 (Oct. 2003), ISSN 0031-9015, <http://jpsj.ipap.jp/link?JPSJ/72/2433/>
- <sup>70</sup> a. Liebsch, H. Ishida, and G. Bihlmayer, *Physical Review B* **71**, 085109 (Feb. 2005), ISSN 1098-0121, <http://link.aps.org/doi/10.1103/PhysRevB.71.085109>

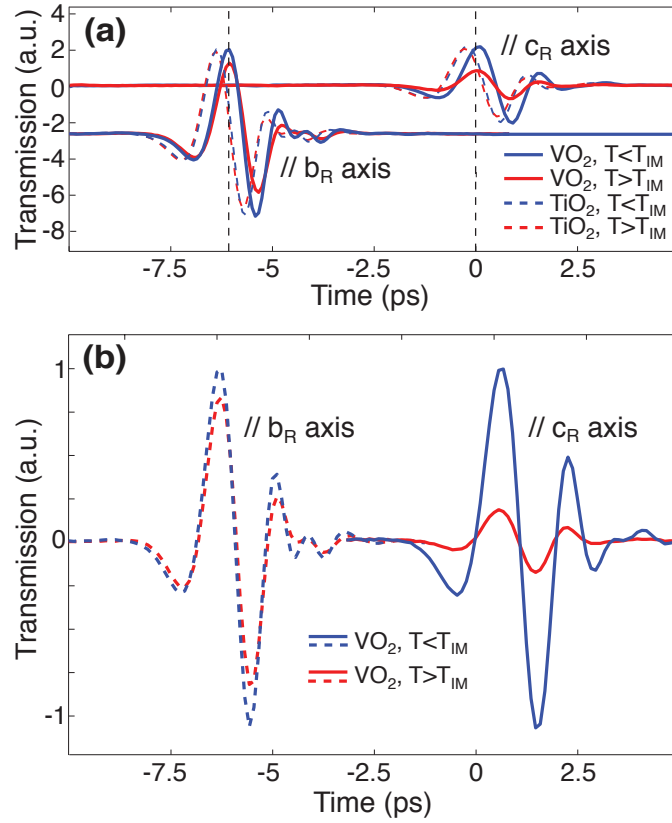


FIG. 1. (a) THz transmission along  $c_R$  and  $b_R$  (vertically offset) in the  $100\text{nm}$   $(100)_R$   $\text{VO}_2$  sample (solid) and in the  $\text{TiO}_2$  reference substrate (dashed), below (blue) and above (red)  $T_{MI}$ . The large refractive index anisotropy of the  $\text{TiO}_2$  substrate leads to a slower propagation of the laser pulse along  $c_R$  than along  $b_R$ , which enables the distinction of the two signals, and thus the orientation of the sample with respect to the incident field polarization. (b) THz transmission along  $c_R$  and  $b_R$  in the  $250\text{nm}$   $(100)_R$   $\text{VO}_2$  sample, below (blue) and above (red)  $T_{MI}$ , normalized to the high temperature value. The relative low temperature transmission along  $b_R$  ( $\sim 85\%$ ) is dramatically different from that along  $c_R$  ( $\sim 15\%$ ).

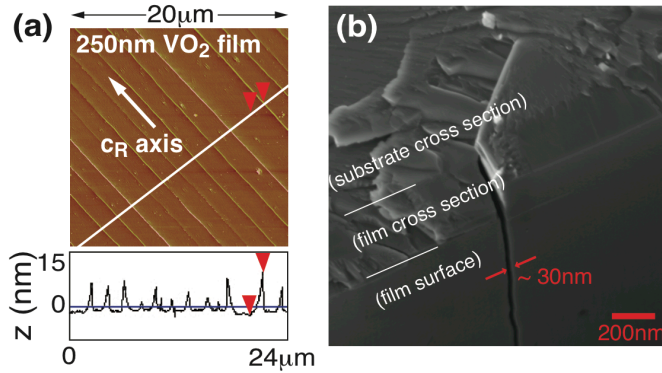


FIG. 2. Characterization of the  $250\text{nm}$  thick  $(100)_R$   $\text{VO}_2$  film. (a) AFM phase image ( $0^\circ$ - $5^\circ$  scale) and corresponding height profile: the  $250\text{nm}$  sample shows buckling induced ridges along  $c_R$  (height indicated by the arrows:  $\Delta z = 14.307\text{nm}$ ). (b) SEM image of a section of the sample (seen from the edge, the surface and the cross section being located as labeled) showing a  $\sim 30\text{nm}$  wide crack.

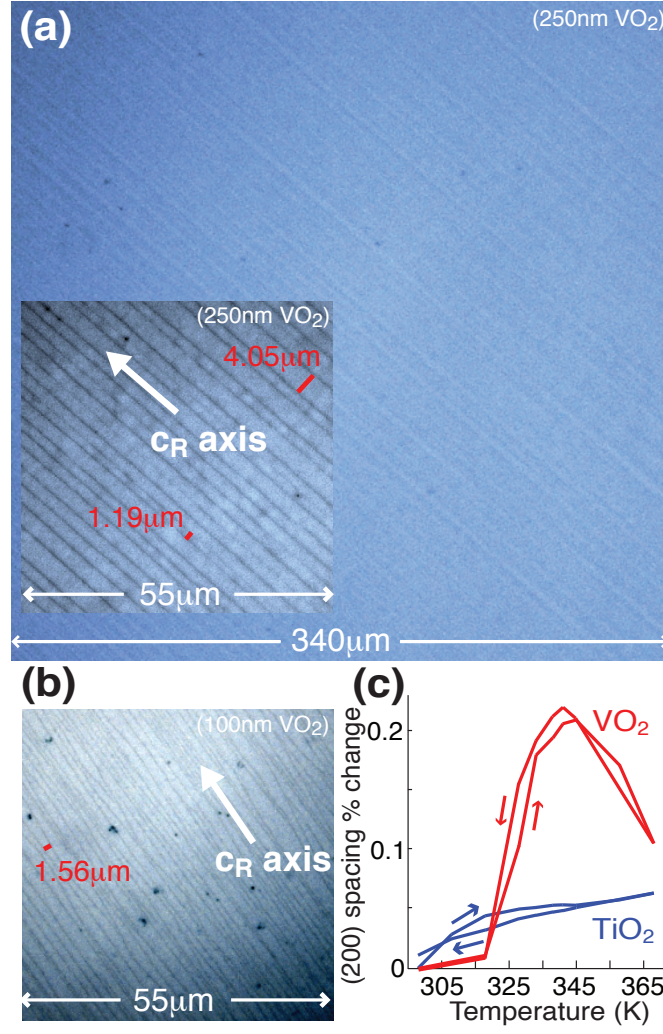


FIG. 3. Characterization of  $\text{VO}_2$  thin films on a  $(100)_R$   $\text{TiO}_2$  substrate. Optical images of the (a) 250nm and (b) 100nm films: the samples show buckling induced ridges along  $c_R$ , spaced by  $\sim 1\mu\text{m}$ . (c) Temperature dependence (for increasing and decreasing temperature) of the a-axis lattice spacing, deduced from XRD data: a  $\sim 0.1\%$  increase is observed along  $a_R$ , in the 100nm thick  $\text{VO}_2$  sample, across the structural transition which occurs at  $T_{St} = 340\text{K}$ . The expected linear increase of the  $a_R$ -axis lattice spacing of  $\text{TiO}_2$  with temperature is also observed.

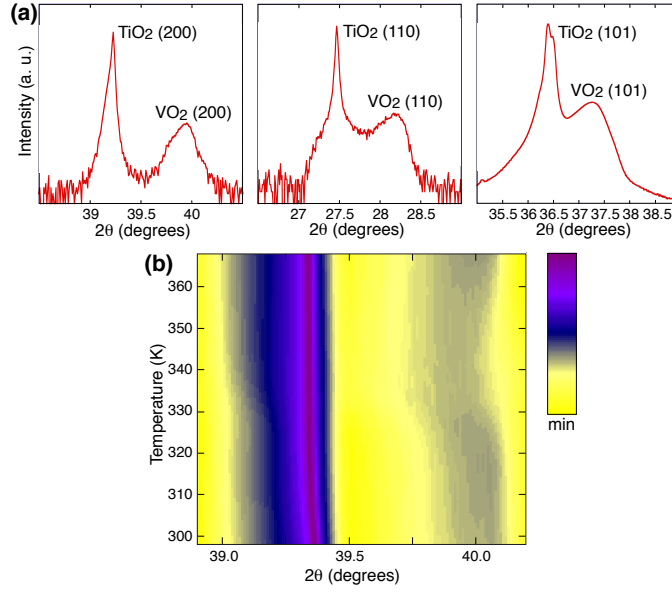


FIG. 4. (a) Room temperature XRD of the 100nm thick VO<sub>2</sub> thin film, along three different directions: (200)<sub>R</sub>, (110)<sub>R</sub>, (101)<sub>R</sub>. The lattice parameters can be estimated as 4.52Å along  $a_R$ , 4.46Å along  $b_R$  and 2.89Å along  $c_R$ , yielding mismatches of  $-0.83\%$  along  $a_R$ ,  $-2.17\%$  along  $b_R$  and  $1.41\%$  along  $c_R$ . (b) Temperature dependent XRD of the 100nm thick VO<sub>2</sub> thin film. Both the TiO<sub>2</sub> and the VO<sub>2</sub> (200)<sub>R</sub> peaks are seen to shift as a function of temperature. There is no evidence of the development of any additional structural phase.

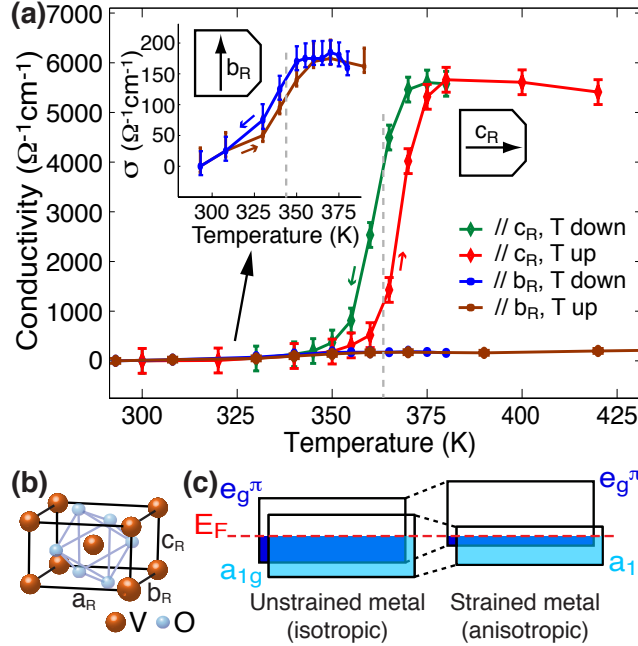


FIG. 5. (a) Temperature dependence of the far infrared conductivity in 100nm (100)<sub>R</sub> VO<sub>2</sub>:  $\sigma_{c_R} \simeq 30\sigma_{b_R}$  above the MIT temperature;  $T_{MI}^{c_R} = 365\text{K}$  while  $T_{MI}^{b_R} = 340\text{K} = T_{MI}^{bulk}$ . (b) The VO<sub>2</sub> rutile unit cell, following Eyert<sup>24</sup>. (c) Effect of tensile strain along  $c_R$  on the electronic structure of metallic VO<sub>2</sub>: antibonding  $e_g^\pi$  bands are shifted upwards while the  $a_{1g}$  band is narrowed.

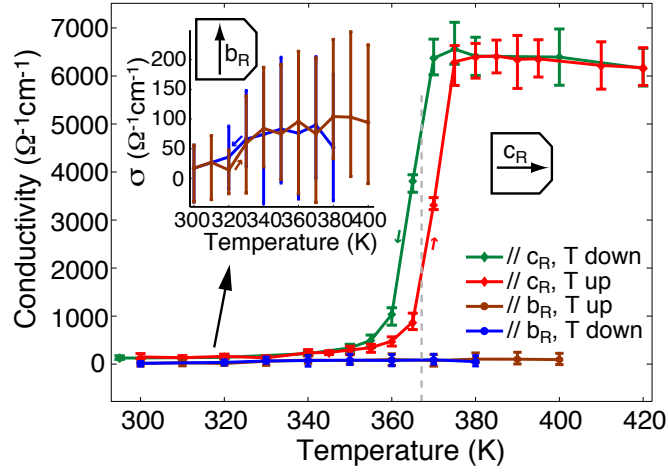


FIG. 6. Temperature dependence of the far-infrared conductivity in  $250\text{nm}$   $(100)_R$   $\text{VO}_2$ :  $\sigma_{c_R} \simeq 5250(\Omega\text{cm})^{-1}$  for  $T > T_{MI}^{c_R} \simeq 365\text{K}$ ;  $\sigma_{b_R} < 100(\Omega\text{cm})^{-1}$  and  $T_{MI}^{b_R}$  can only be estimated as  $T_{MI}^{b_R} \simeq 340\text{K}$ .

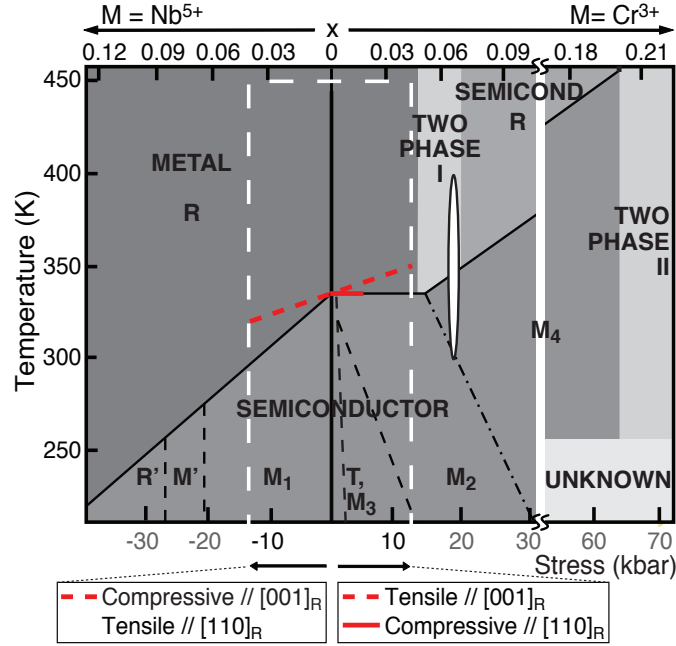


FIG. 7. Phase diagram of  $\text{VO}_2$  for stress applied mostly along  $[110]$ . The black solid line indicates  $T_{MI}$ ; the white oval defines the phase space of our samples; uniaxial stress results are presented in the region delimited by the dashed white lines; doping ( $\text{V}_{1-x}\text{M}_x\text{O}_2$ ) leading to reduction ( $\text{M}=\text{Nb}^{5+}$ ) or oxidation ( $\text{M}=\text{Cr}^{3+}$ ) of  $\text{V}^{4+}$  is specified on the top horizontal axis<sup>17,29–33</sup> (refer to the main text for more details).



publication	sample type	method	anisotropy below $T_{MI}$	anisotropy above $T_{MI}$
Bongers <i>et al.</i> (1965)	bulk single crystal (needle along $c_R$ , 6x0.3x0.15mm)	two-probe	2	2.5
Barker <i>et al.</i> (1966)	bulk polycrystal (well defined $c_R$ )	Hall voltage	0.7-0.8	1.1-2
Kosuge <i>et al.</i> (1967)	bulk single crystal	two-probe	1.14	0.58
Koide <i>et al.</i> (1967)	single crystal film on rutile substrate	two probe	2	0.001-0.1
	bulk single crystal (needle along $c_R$ , 3x0.8x0.07mm)	two-probe	< 1.2	0.33
Everhart <i>et al.</i> (1968)	bulk single crystal (4-7x1-4x1-4mm)	four-probe	2-10	7.5
Verleur <i>et al.</i> (1968)	bulk single crystal	reflectivity (0.25-5eV)	0.28-1.4	0.79-2
Continenza <i>et al.</i> (1999)	(calculations)	model GW (0-10eV)	3-6.7	N/A
Mossaneck <i>et al.</i> (2007)	(calculations)	LDA (0-12eV)	0.6-> 3	0.7-3.3
Lysenko <i>et al.</i> (2007)	30nm film on (012) $Al_2O_3$	optical (400nm) diffraction	1.05	1
Lu <i>et al.</i> (2008)	40nm film on (011) $_R$ $TiO_2$	star-shaped electrodes	5.14	1
Tomczak <i>et al.</i> (2009)	(calculations)	LDA+CDMFT (0-5eV)	0.73-1.67	0.96-1.14
our results (2010)	100nm film on (100) $_R$ $TiO_2$	THz TDS (far infrared)	N/A	~30

TABLE I. Compilation of previous experimental and theoretical results for the conductivity (DC, unless otherwise specified) anisotropy,  $\frac{\sigma_{cR}}{\sigma_{bR}}$  or  $\frac{\sigma_{cR}}{\sigma_{aR}}$ , in  $VO_2$ , above and below  $T_{MI}$ , when no external stress is applied.<sup>12,36-39,60-64</sup>

publication	sample type	applied pressure	conductivity vs. pressure	conductivity along...	$dT_{MI}/dP$ [K/kbar]	$dT_{MI}/dP$ along...
Minomura <i>et al.</i> (1964)	bulk	uniaxial (Drickamer cell, up to 160kbar)	not specified	not specified	-0.46	not specified
Neuman <i>et al.</i> (1964)	single crystal	hydrostatic (up to 6kbar)	increases below $T_{MI}$	not specified	no significant change	not specified
	powder	hydrostatic (up to 6kbar)	increases	not specified	no significant change	not specified
Berglund <i>et al.</i> (1969)	bulk single crystal (0.25x0.25x0.2in, crack along $c_R$ )	hydrostatic (up to 44kbar)	increases; saturates above $T_{MI}$ , at 15-20kbar	$c_R$	0.082	$c_R$
Ladd <i>et al.</i> (1969)	bulk single crystal (10x1x1mm)	hydrostatic (up to 8kbar)	increases (up to 30kbar, at $T_{room}$ )	$c_R$	0.06	$c_R$
		along $a_R$ or $b_R$	N/A	$c_R$	no significant change	$c_R$
		along $c_R$ (up to 0.5kbar)	increases below $T_{MI}$	$c_R$	-1.2	$c_R$
Pouget <i>et al.</i> (1975)	bulk single crystal (0.5mm <sup>2</sup> x2mm, 3mm <sup>2</sup> x4mm)	along $[110]_R$ (up to 1.2kbar)	no significant change	$c_R$	no significant change	$c_R$
Gregg <i>et al.</i> (1997)	thin films on Al <sub>2</sub> O <sub>3</sub> (012)	in-plane (3-point bend)	increases below $T_{IM}$	not specified	N/A	N/A
Muraoka <i>et al.</i> (2002)	10-15nm thick single crystal thin films on (001) <sub>R</sub> and (110) <sub>R</sub> TiO <sub>2</sub>	along $c_R$ (epitaxial: -0.3% for (001) <sub>R</sub> , 1.2% for (110) <sub>R</sub> )	increases	$a_R$ or $b_R$ for $[001]_R$ ; not specified for $[110]_R$	< 0	$a_R$ or $b_R$ for $[001]_R$ ; not specified for $[110]_R$
Arcangeletti <i>et al.</i> (2007)	single crystal (5μm thick slab)	uniaxial (diamond a. c., up to 140kbar)	increases below $T_{MI}$ (750-6000cm <sup>-1</sup> )	not specified	N/A	N/A
Lu <i>et al.</i> (2008)	single crystal thin film on (011) <sub>R</sub> TiO <sub>2</sub>	in-plane (epitaxial: -1.2%///[011] <sub>R</sub> , -0.4%///[001] <sub>R</sub> )	N/A	$a_R$ or $b_R$	< 0	$a_R$ or $b_R$
Sakai (2008)	polycrystalline thin film on metallic Ti ( $a_R$ in plane)	in-plane (point contact, up to 255kbar)	increases	not specified	> 0	not specified
Cao <i>et al.</i> (2009)	single crystal (0.5-2x0.5-2x100 nm, along $c_R$ )	along $c_R$ (3-point bend, up to 12kbar)	increases (optical)	$c_R$	~-2	$c_R$
our results (2010)	single crystal thin film on (100) <sub>R</sub> TiO <sub>2</sub>	in-plane (epitaxial: 5.4%///[001] <sub>R</sub> , -2.3%///[010] <sub>R</sub> )	no significant change (far IR))	$c_R$	< 0	$c_R$
			decreases above $T_{MI}$ (far IR)	$b_R$	no significant change	$b_R$

TABLE II. Compilation of previous experimental and theoretical results for the variation of  $T_{MI}$  and of the conductivity (DC, unless otherwise specified) in VO<sub>2</sub>, under applied hydrostatic or uniaxial pressures. We assume  $\Delta P > 0$  for compression and  $\Delta P < 0$  for expansion.<sup>1,7,11,12,17,29,40,41,65-67</sup>